AGU PUBLICATIONS

JGR

Journal of Geophysical Research: Space Physics

RESEARCH ARTICLE

10.1002/2014JA019781

Key Points:
- The methane homopause is most likely near 1000 km altitude
- Hydrodynamic escape of methane is not required to match INMS
- Molecular hydrogen is best fit with a methane homopause of 1000 km

Correspondence to:
J. M. Bell,
jared.m.bell@gmail.com

Citation:
Bell, J. M., J. Hunter Waite Jr., J. H. Westlake, S. W. Bougher, A. J. Ridley, R. Perryman, and K. Mandt (2014), Developing a self-consistent description of Titan's upper atmosphere without hydrodynamic escape, *J. Geophys. Res. Space Physics*, *119*, 4957–4972, doi:10.1002/2014JA019781.

Received 10 JAN 2014
Accepted 16 MAY 2014
Accepted article online 24 MAY 2014
Published online 13 JUN 2014

Developing a self-consistent description of Titan's upper atmosphere without hydrodynamic escape

Jared M. Bell[1], J. Hunter Waite Jr.[2,3], Joseph H. Westlake[4], Stephen W. Bougher[5], Aaron J. Ridley[5], Rebecca Perryman[2], and Kathleen Mandt[2]

[1]Center for Planetary Atmospheres and Flight Sciences, National Institute of Aerospace, Hampton, Virginia, USA, [2]Division of Space Science and Engineering, Southwest Research Institute, San Antonio, Texas, USA, [3]Department of Physics and Astronomy, University of Texas at San Antonio, San Antonio, Texas, USA, [4]Johns Hopkins University Applied Physics Laboratory, Michigan, USA, [5]Department of Atmospheric, Oceanic, and Space Sciences, University of Michigan, Ann Arbor, Michigan, USA

Abstract In this study, we develop a best fit description of Titan's upper atmosphere between 500 km and 1500 km, using a one-dimensional (1-D) version of the three-dimensional (3-D) Titan Global Ionosphere-Thermosphere Model. For this modeling, we use constraints from several lower atmospheric Cassini-Huygens investigations and validate our simulation results against in situ Cassini Ion-Neutral Mass Spectrometer (INMS) measurements of N_2, CH_4, H_2, ^{40}Ar, HCN, and the major stable isotopic ratios of $^{14}N/^{15}N$ in N_2. We focus our investigation on aspects of Titan's upper atmosphere that determine the amount of atmospheric escape required to match the INMS measurements: the amount of turbulence, the inclusion of chemistry, and the effects of including a self-consistent thermal balance. We systematically examine both hydrodynamic escape scenarios for methane and scenarios with significantly reduced atmospheric escape. Our results show that the optimum configuration of Titan's upper atmosphere is one with a methane homopause near 1000 km and atmospheric escape rates of $1.41–1.47 \times 10^{11}$ CH_4 m^{-2} s^{-1} and 1.08×10^{14} H_2 m^{-2} s^{-1} (scaled relative to the surface). We also demonstrate that simulations consistent with hydrodynamic escape of methane systematically produce inferior fits to the multiple validation points presented here.

1. Introduction

Atmospheric loss of constituents to space is a major process by which atmospheres evolve over time [*Yung and Demore*, 1999]. Titan is unique in the solar system because it is the only terrestrial body besides Earth that has a substantial N_2-dominated atmosphere, making it a possible analogue for an early, prebiotic Earth [cf. *Clarke and Ferris*, 1997; *Sagan and Thompson*, 1984; *Yung et al.*, 1984]. Thus, understanding Titan's atmospheric evolution is key to determining how Earth's atmosphere may have transitioned into its current state [*Yung and Demore*, 1999]. Models that describe Titan's atmospheric evolution are sensitive to the assumed atmospheric escape rates of methane (CH_4) and molecular hydrogen (H_2) over geologic time [e.g., *Mandt et al.*, 2009; *Mandt et al.*, 2012; *Lorenz et al.*, 1999]. Therefore, quantifying current atmospheric escape rates is central to understanding the evolutionary trajectory of Titan's atmosphere. And, more broadly, this quantification may provide clues about how Earth's atmosphere evolved into its current life-sustaining environment.

Unfortunately, direct measurements of neutral atmospheric escape are not made by instruments on the Cassini orbiter and there are currently no published constraints on neutral methane escape from magnetospheric measurements. Thus, we must rely upon numerical models, usually one-dimensional (1-D), to infer atmospheric escape rates from Titan. These 1-D models are constrained to simultaneously match atmosphere composition below 500 km and Cassini Ion-Neutral Mass Spectrometer (INMS) data above 1000 km. Key parameters, such as eddy diffusion and topside escape rates, are then adjusted until the simulated densities and mixing ratios match INMS data.

Using this approach, *Strobel* [2009], *Yelle et al.* [2008], and *Cui et al.* [2012] estimated that large escape rates of methane (between ~2.0 and 3.0×10^{13} CH_4 m^{-2} s^{-1} or ~40 and 60 kg s^{-1} globally) are required to reproduce the INMS composition measurements. *Strobel* [2008, 2009] concluded that these inferred atmospheric escape rates of CH_4 were evidence of hydrodynamic escape. Conversely, several studies have suggested that hydrodynamic escape rates of CH_4 are not required to match INMS data. *Tucker and Johnson* [2009], and

Table 1. Global Parameter Settings for 1-D T-GITM

Parameter	Setting in T-GITM
$F_{10.7-cm}$ radio flux	80.0×10^{-22} W/m^2/Hz
Solar zenith angle	60°
Saturn-Sun radial distance	9.25 AU
Model radial resolution	10 km

Tucker et al. [2013], using a direct simulation Monte Carlo method, have reproduced the INMS measurements in the upper atmosphere while using only thermal escape rates of methane (less than 1.0×10^9 CH_4 m^{-2} s^{-1}). Similarly, *Bell et al.* [2010a, 2010b, 2011b] used a 1-D version of the Titan Global Ionosphere-Thermosphere Model (T-GITM) to reproduce the INMS densities and mixing ratios using a methane homopause near 1000 km and escape rates of $\sim 1.0 \times 10^8$ CH_4 m^{-2} s^{-1}.

This methane escape controversy is mirrored by an apparent mismatch between the INMS H_2 density and mixing ratio measurements and those made by the Composite InfraRed Spectrometer (CIRS) and Gas Chromatograph Mass Spectrometer (GCMS) investigations below 200 km. *Cui et al.* [2008] and *Strobel* [2009] demonstrated that H_2 densities and mixing ratios measured by INMS could be simulated using escape rates consistent with a limiting flux mechanism [*Hunten*, 1974], where upwelling H_2 from the lower atmosphere is limited through the homopause region. While most studies agree on the H_2 escape rates, *Strobel* [2010, 2012] found that 1-D simulations could not simultaneously match both the INMS H_2 measurements and those of CIRS and GCMS. Moreover, *Strobel* [2012] concluded that this mismatch between the INMS H_2 measurements above 1000 km and those below 200 km is exacerbated when using the high-methane homopause and low-methane escape rates of *Bell et al.* [2010b, 2011b].

Thus, our goal in this manuscript is to address simultaneously the controversy in CH_4 escape rates and the apparent mismatch between the upper and lower atmosphere H_2 composition measurements. We will do this by building upon our previous work in *Bell et al.* [2010a, 2010b, 2011b], where we identified three key aspects of our 1-D simulations that determined the amount of atmospheric escape of CH_4 and H_2 needed to match INMS measurements: (1) the amount of turbulence used in the model, (2) the net chemical destruction of methane (net production of H_2) included in the model (i.e., the sum over direct photolytic, ion-neutral, and neutral-neutral chemical losses), and (3) the inclusion of a self-consistent thermal balance calculation. We have designed a series of numerical experiments that explore each of these aspects sequentially, building from highly simplified simulations to fully coupled simulations that combine all three aspects into a global mean description of Titan's upper atmosphere.

Our efforts here differ significantly from our work in *Bell et al.* [2010a, 2010b, 2011b]. Previously, we accounted for both diurnal and sun-Saturn orbital distance variations over the course of our simulations, which are not accounted for in the collective works of *Cui et al.* [2008], *Strobel* [2008, 2009, 2010, 2012], and *Yelle et al.* [2008]. To address these differences, we now focus on a series of simulations that approximate a global mean state during the TA-T40 timeframe, by specifying a fixed solar zenith angle of 60°, an orbital distance of 9.25 AU, and an $F_{10.7-cm}$ flux that we divide by 2.0 (see Table 1). Using this global mean configuration, we present a sequence of 1-D T-GITM simulations that are more directly comparable with other studies on atmospheric escape. Our investigation demonstrates that the lower atmosphere and upper atmosphere measurements of N_2, CH_4, H_2, $^{14}N/^{15}N$, HCN, and ^{40}Ar can be simultaneously explained in a single theoretical description of Titan's upper atmosphere from 500 to 1500 km. Moreover, we find that the best fit description of the INMS CH_4 and H_2 measurements is obtained when using a high-methane homopause configuration without hydrodynamic escape of CH_4.

2. The T-GITM Framework

The Titan Global Ionosphere-Thermosphere Model (T-GITM) is a three-dimensional (3-D) nonhydrostatic global circulation model (GCM) that solves the time-dependent Navier-Stokes equations between 500 km and 1500 km on a spherical altitude grid (see Appendix A for more details). The T-GITM numerical solvers in the vertical (i.e., radial) direction have been updated to use the Advection Upstream Splitting Method (AUSM$^+$-up) of [*Liou*, 2006] as well as the fourth-order Runge-Kutta time-stepping scheme outlined in *Ullrich and Jablonowski* [2012]. T-GITM currently carries 15 neutral species (N_2, CH_4, ^{40}Ar, HCN, H_2, $^{13}CH_4$, ^{15}N-^{14}N, N(^{4}S), H, C_2H_4, $^3CH_2$, $^1CH_2$, CH_3, CH, and H_2CN), five ion species (N_2^+, N^+, $HCNH^+$, CH_3^+, and $C_2H_5^+$), and electrons equal to the total ion content to provide charge neutrality.

All species are coupled through a reduced ion-neutral chemical scheme that focuses on the formation of HCN [*Bell et al.*, 2010a]. However, this chemical scheme does not liberate the amount of H_2 inferred from

Table 2. T-GITM Lower Boundary Settings at 500 km Altitude and Cassini-Huygens Constraints

T-GITM Lower Boundary Field	Cassini-Huygens Range
$\chi_{CH_4} = 1.48\%$	$1.48 \pm 0.9\%$ (GCMS[a]) and $1.6 \pm 0.5\%$ (CIRS[b])
$\chi_{H_2} = 2.00 \times 10^{-3}$	$1.0 \pm 0.5 \times 10^{-3}$ (CIRS[c]) and $1.01 \pm 0.16 \times 10^{-3}$ (GCMS[a])
$\chi_{Ar^{40}} = 3.30 \times 10^{-5}$	$3.39 \pm 0.12 \times 10^{-5}$ (GCMS[a])
$^{14}N/^{15}N = 167.7$	167.7 ± 0.6 (GCMS[a])
$T = 175.0$ K	160.0–190.0 (CIRS[e])
$n = 9.0 \times 10^{19}$ (m^{-3})	$\sim 8.2 \times 10^{19}$ (m^{-3}) (HASI[f])

[a] *Niemann et al.* [2010].
[b] *Flasar et al.* [2005].
[c] *Jennings et al.* [2009].
[d] *Teanby et al.* [2007].
[e] *Achterberg et al.* [2008].
[f] *Fulchignoni et al.* [2005].

an analysis of the Cassini INMS heavy hydrocarbon data by *Waite et al.* [2007] and *Westlake et al.* [2012], which indicate that the heavy hydrocarbons have a carbon to hydrogen ratio of roughly 1:1.7. This 1:1.7 C to H ratio suggests that 1.15 H_2 molecules are liberated for every CH_4 molecule consumed by chemistry. We approximate this amount of H_2 production by employing a semiempirical H_2 production rate in the T-GITM continuity equation given by $P_{H_2} = 1.15 \times L_{CH_4}$. While this approach is ad hoc, we examine the sensitivity of the simulated H_2 to chemistry in section 5.

For the purposes of simplicity, we perform 1-D T-GITM simulations that have identical orbital, seasonal, and solar cycle settings, which are outlined in Table 1 and are consistent with a global average. The 1-D simulations have a uniform 10 km vertical resolution and have a specified 60° solar zenith angle. We approximate a diurnal average by dividing the solar fluxes by a factor of 2.0. This approach differs from the settings in *Bell et al.* [2010a, 2010b, 2011b], but it matches other 1-D investigations of Titan's upper atmosphere [e.g., *Krasnopolsky*, 2009, 2010; *Strobel*, 2010; *Yelle et al.*, 2008].

T-GITM uses two layers of ghost cells (or boundary cells) for calculating gradients and specifying boundary conditions at the edges of the physical domain. At the lower boundary, we specify fixed densities and temperatures consistent with the Cassini-Huygens measurements listed in Table 2. However, for photochemically produced species, such as HCN, C_2H_4, and $N(^4S)$, we do not specify a fixed mixing ratio at 500 km, since (1) there are few reliable constraints and (2) doing so could bias their simulated densities. Instead, for these three photochemical species we extend the mixing ratios downward from the physical regime into the boundary cells. This approach allows the combined vertical dynamics and integrated chemistry to determine the mixing ratios in the T-GITM simulations. At the upper boundary (1500 km), we extend the temperatures and densities from the physical calculation domain into the boundary cells.

For the vertical velocities of most species, we do not specify boundary conditions at either boundary and we simply extend the velocities downward and upward from the calculation domain. For light species, such as H and H_2, we calculate their classical Jeans escape velocities at 1500 km in order to capture their thermal escape. Moreover, we specify hydrodynamic escape velocities of CH_4 in some simulations and we impose this escape by forcing a flux condition on either the lower or upper boundary of the model.

3. The Data Sets Used

In this section, we outline the key aspects of the INMS data used to infer atmospheric escape rates. There are currently two peer-reviewed methods for analyzing the INMS raw data: (1) the methods developed by *Magee et al.* [2009] and (2) the methods developed by *Cui et al.* [2008] and *Cui et al.* [2012]. Both methods produce similar results for the major species densities but differ in their minor species composition. For the purposes of this investigation, we rely on results obtained using the methods of *Magee et al.* [2009], but we emphasize that either method could be used with equal validity. In order to correct for a systematic underestimate of the neutral densities relative to other investigations, the INMS neutral densities have been multiplied by a uniform factor of 2.7 [*Bell et al.*, 2010b]. Moreover, we average the flyby densities

between TA and T40 to create a prime mission average, properly propagating both the counting statistical and geophysical variabilities into our averages [*Bell et al.*, 2010a, 2010b].

Our fixed simulation settings outlined in Table 1 are roughly consistent with the mean conditions of the Cassini Prime Phase between TA and T40, which according to *Westlake et al.* [2011] has a mean solar zenith angle of ~103°, $F_{10.7-cm}$ value of 75 $\times 10^{-22}$ W m^{-2} s^{-1} Hz^{-1}, a mean latitude of ~36.6°N, and Sun-Saturn distance of roughly 9.20 AU. Ideally, we should run 3-D T-GITM simulations that account for the different flyby trajectories, at different orbital positions, and with more precise solar flux values. However, our main objective is to generate 1-D simulations that are (1) more directly comparable with other 1-D efforts and (2) representative of a global mean state of Titan's atmosphere during the TA–T40 timeframe.

In order to validate T-GITM, we calculate arithmetic mean deviations between simulated densities and mixing ratios and the INMS measurements:

$$\text{Percent deviation} = 100 \times \sum_i \frac{\psi^i_{\text{GITM}} - \psi^i_{\text{INMS}}}{\psi^i_{\text{INMS}}}, \tag{1}$$

where ψ represents a specific mixing ratio or density, the subscript GITM denotes a model field, INMS the data field, and the index "*i*" ranges over the altitudes between 1050 km and 1500 km. We interpolate the INMS data and uncertainties onto the T-GITM uniform 10 km grid between 1050 km and 1500 km.

4. T-GITM Simulation Results

In the following four subsections, we outline a series of T-GITM simulations that systematically isolate and investigate the different processes that impact atmospheric escape. In sections 4.1–4.3, we begin with simulations that have a specified thermal structure that is unchanging over the course of the simulation (i.e., we omit the energy balance calculations). In section 4.1, we examine how the method for including turbulence impacts simulated mixing ratios of ^{40}Ar—a key tracer of eddy diffusion. In section 4.2, we isolate the impacts of varying the amount of turbulence in T-GITM simulations. Section 4.3 outlines the impacts of either including or omitting chemical losses of CH_4 on our estimates of atmospheric escape. Finally, in section 4.4, we introduce Navier-Stokes simulations that include fully coupled composition, momentum, and energy balance calculations.

4.1. Examining Different Eddy Diffusion Formulations

Eddy diffusion is a heuristic parameter that approximates the effects of subgrid scale turbulence on atmospheric models [see *Atreya*, 1986]. In T-GITM, this parameter obeys the following formula:

$$K_E(r) = K_0 \sqrt{\frac{N_0}{N(r)}}, K_E(r) \leq K_{\text{Max}}, \tag{2}$$

where K_E is the eddy diffusion coefficient (in m^2 s^{-1}), K_0 is the reference coefficient at the model lower boundary, $N(r)$ is the total neutral density (in m^{-3}), K_{Max} is the upper limit on eddy diffusion that we can adjust to enforce a desired homopause altitude, and N_0 is the total density at 500 km. As noted in *Krasnopolsky* [2009], this functional form approximates the effects of upward propagating gravity waves. By adjusting the upper limit, K_{Max}, the eddy diffusion coefficient will dictate the amount of mixing in the atmosphere and the altitude at which the atmosphere goes from a well-mixed state to a molecular diffusive state—the homopause.

As found in *Bell et al.* [2010a, 2010b, 2011b], *Yelle et al.* [2008], and *Strobel* [2012], changing the magnitude of the eddy diffusion coefficient will significantly impact the amount of atmospheric escape of CH_4 required by models to reproduce the INMS densities and mixing ratios. Thus, a method for reliably capturing the effects of this turbulence is central to inferring atmospheric escape. Since Cassini's arrival to the Saturnian system, INMS densities and mixing ratios have been used to constrain the amount of turbulence in the upper atmosphere. In particular, *Yelle et al.* [2008] suggested that INMS measurements of ^{40}Ar could act as a tracer in numerical models.

Because of this, we use ^{40}Ar mixing ratios to benchmark the eddy diffusion coefficient used in T-GITM simulations. However, various modeling studies incorporate eddy diffusion using different methods. Thus, for a given eddy diffusion coefficient, we must test whether or not we obtain the same simulated vertical profile of ^{40}Ar mixing ratios when using different numerical methods. In order to investigate this, we consider

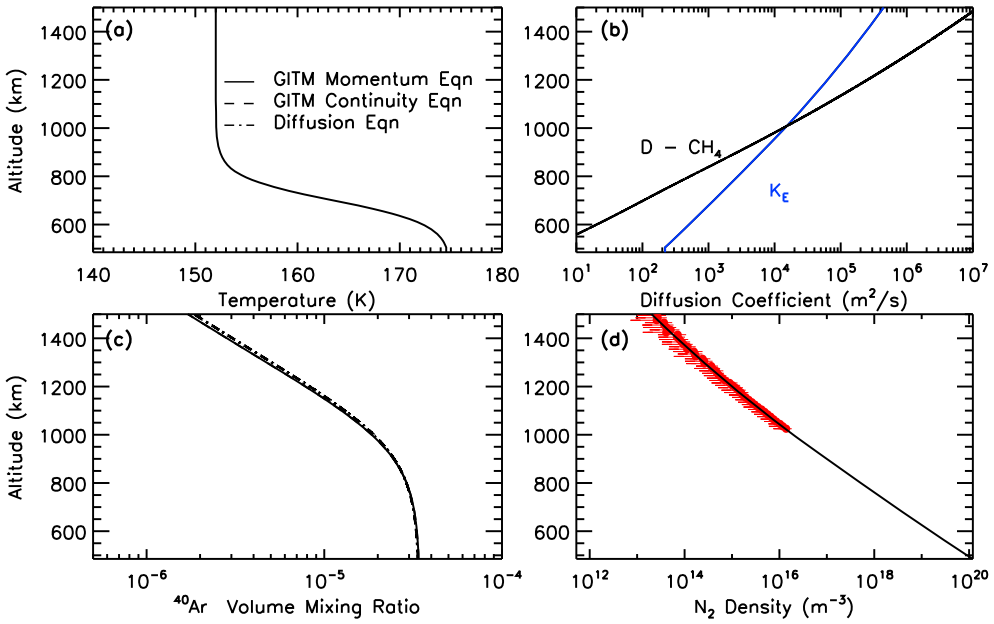

Figure 1. Three methods for including turbulence (eddy diffusion) into T-GITM: the momentum equation (solid), the continuity equation (dashed), and the hydrostatic diffusion model (dash-dotted). (a) The neutral temperatures, (b) the molecular diffusion coefficients (black) and eddy diffusion coefficients (blue), (c) the effects of eddy diffusion on ^{40}Ar mixing ratios, and (d) neutral densities (black) with INMS data of *Magee et al.* [2009] in red.

three methods (see Appendix A) for including turbulence in 1-D simulations: (1) the hydrostatic diffusion approach of *Yelle et al.* [2006, 2008] and *Cui et al.* [2012], (2) the inclusion of turbulence in the continuity equation like *Strobel* [2008, 2009, 2010, 2012], and (3) the inclusion of turbulence in the momentum equation like *Bell et al.* [2010a].

Figure 1 shows a comparison among the three methods for turbulence. These three simulations share the same composition and eddy diffusion constraints. Moreover, the temperatures are specified at all times in the simulations. Thus, only the method for including turbulence varies among these three simulations. Figure 1a depicts the specified thermal structure used in all three simulations, and Figure 1d depicts the simulated N_2 neutral densities (black lines) along with the INMS N_2 densities (red circles and horizontal uncertainties). Figure 1b contains the molecular diffusion coefficient of CH_4 (in black) and the assumed eddy diffusion coefficients (in blue). As seen in Figure 1c, the effects of eddy diffusion on ^{40}Ar mixing ratios are very consistent among all methods and any differences between the simulated mixing ratios are less than 5%. This demonstrates that the simulated effects of eddy diffusion are method independent. Based upon this result, we will continue to include the effects of eddy diffusion in the momentum equation.

4.2. Eddy Diffusion: Homopause

Next, we isolate the impacts of varying the eddy diffusion coefficient on the inferred methane escape rates in T-GITM simulations. In order to do this, we consider two broad cases of eddy diffusion: (1) a low-methane homopause case near 880 km (consistent with *Strobel* [2009], *Yelle et al.* [2008], and *Cui et al.* [2012]) and (2) a high-methane homopause case near 1000 km (consistent with *Bell et al.* [2010b] and *Mandt et al.* [2012]). To test these methane homopause cases, we introduce three T-GITM simulations: model A, a high-homopause simulation; model B, a low-homopause simulation; and model B (HE), a low-homopause simulation with hydrodynamic escape imposed as a boundary condition because T-GITM cannot self-consistently calculate it. As in section 4.1, these three T-GITM simulations share the same fixed thermal structure of Figure 1a, which means that no energy balance calculations are performed. Models A, B, and B (HE) also share the same lower boundary constraints and the same chemical scheme. Thus, only the eddy diffusion coefficient and topside escape rates vary among these simulations.

The key characteristics of models A, B, and B (HE) are summarized in Table 3, and the resulting fields are presented in Figures 2 and 3. In this table, we highlight the topside escape rates for CH_4 and H_2 (scaled relative to the surface of Titan), the integrated chemical destruction of CH_4 (scaled relative to the surface of Titan),

Table 3. T-GITM Simulation Parameters (Fluxes/Integrated Values Scaled Relative to Surface)

	Φ_{CH_4} ($CH_4/m^2/s$)	Φ_{H_2} ($H_2/m^2/s$)	Integrated Chemical Loss ($CH_4/m^2/s$)	K_{max} (m^2/s)	CH_4 Homopause Altitude (km)
Section 4.1: Eddy diffusion tests with frozen temperatures					
Model A	1.41×10^{11}	1.08×10^{14}	5.13×10^{13}	10^6	~990 km
Model B	3.15×10^{11}	1.10×10^{14}	5.14×10^{13}	1750.0	~880 km
Model B (HE)[a]	2.60×10^{13}	1.08×10^{14}	5.14×10^{13}	1750.0	~880 km
Section 4.2: Methane chemistry tests with frozen temperatures					
Model A	1.41×10^{11}	1.08×10^{14}	5.13×10^{13}	10^6	~990 km
Model A (NC)[b]	1.10×10^{11}	1.08×10^{14}	(No chemistry)	10^6	~990 km
Model A (NC HE)[ab]	1.71×10^{13}	1.08×10^{14}	(No chemistry)	10^6	~990 km
Section 4.3: Energy balance calculations with $Q_{Plasma} = 3.04 \times 10^9$ ($eV/cm^2/s$)					
Model C	1.47×10^{11}	1.07×10^{14}	5.14×10^{13}	10^6	~990 km
Model D	2.55×10^{11}	1.10×10^{14}	5.11×10^{13}	1750.0	~880 km
Model D (HE)[a]	2.49×10^{13}[a]	1.09×10^{14}	5.04×10^{13}	1750.0	~880 km

[a](HE) means hydrodynamic escape rates are specified as a boundary condition.
[b](NC) means that simulation neglects methane chemical losses.

K_{Max} values, and the homopause altitudes for each T-GITM simulation. Operationally, we obtain different methane homopause altitudes by adjusting the K_{Max} values, where the low-homopause altitudes of 880 km correspond to $K_{Max} = 1750\ m^2\ s^{-1}$ and the high-methane homopause altitude of 990 km corresponds to $K_{Max} = 1.0 \times 10^6\ m^2\ s^{-1}$. Additionally, all simulations share the same K_0 values and the same functional form given by equation (2). Finally, Table 4 summarizes how these models compare with the INMS data, based upon the percent deviation outlined above in equation (1).

Figure 2 summarizes the major composition results from these three simulations. Figures 2a and 2b show the simulated major neutral densities and mixing ratios, respectively. The black lines represent T-GITM simulations, and the red circles represent the average INMS measurements during the prime mission as determined by *Magee et al.* [2009] (please note that horizontal uncertainties are a convolution of both counting statistical uncertainties and geophysical variabilities). The CIRS and GCMS ranges for these species

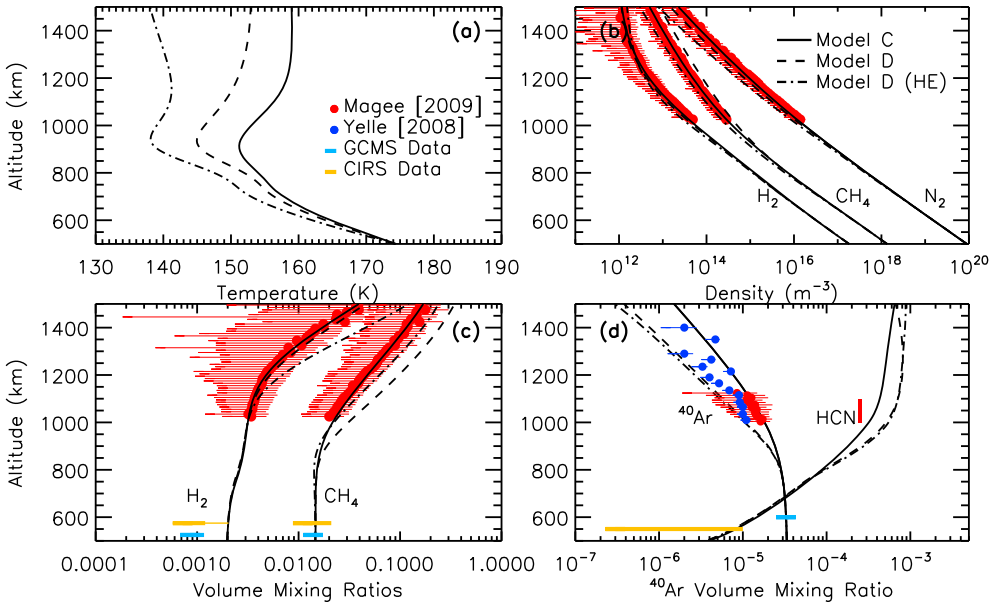

Figure 2. T-GITM simulations with different methane homopause altitudes: models A, solid; B, dashed; and B (HE), dash-dotted. Red data are from *Magee et al.* [2009], and dark blue points are from *Yelle et al.* [2008]. The cyan and yellow data represent GCMS and CIRS constraints, respectively. (a) Neutral temperatures, (b) neutral densities, (c) volume mixing ratios of methane and hydrogen, and (d) volume mixing ratios of HCN and Argon.

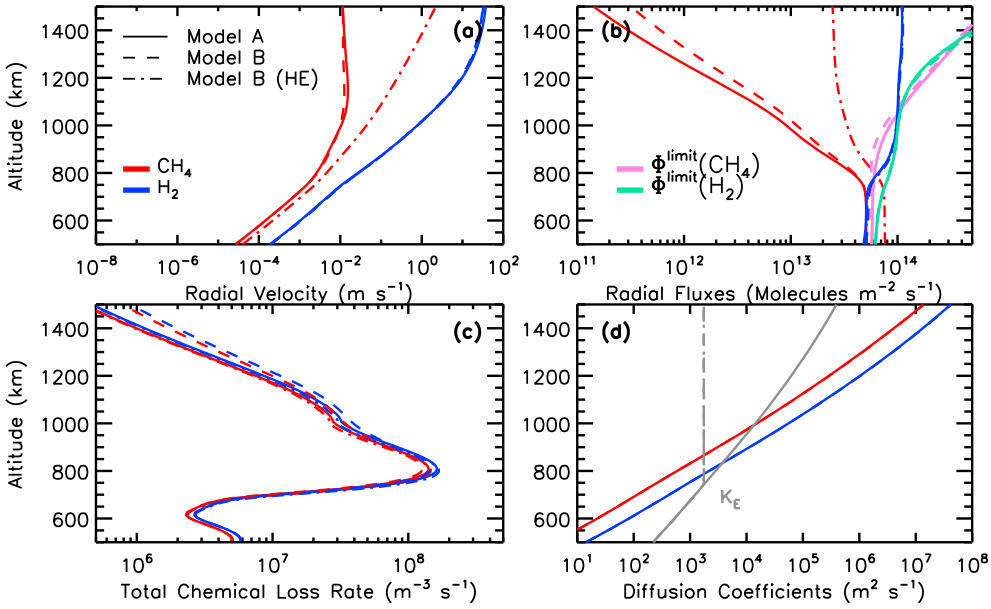

Figure 3. Dynamical fields from models A, solid; B, dashed; and B (HE), dash-dotted. Species are color coded: CH_4, red; and H_2, blue. Total chemical loss rates represent the summation over all chemical loss mechanisms (for CH_4) or production mechanisms (for H_2). (a) The radial (vertical) velocities of methane and hydrogen, (b) their radial fluxes, (c) their total chemical losses, and (d) their molecular diffusion coefficients–note that the eddy diffusion coefficient is included as the gray curve.

are shown as horizontal yellow and cyan bars, respectively. Figure 2c shows the T-GITM simulated ^{40}Ar mixing ratios (black) lines and the INMS measurements reported by *Magee et al.* [2009] (red circles with horizontal uncertainties) and those of *Yelle et al.* [2008] (blue circles and horizontal uncertainties). Similarly, Figure 2d shows the simulated and measured major stable isotopic ratios of $^{14}N/^{15}N$ in N_2.

From Figures 2a and 2b and Table 4, we note that the methane densities and mixing ratios simulated by models A and B (HE) reproduce the INMS measurements equivalently well, whereas model B produces a significantly inferior fit to the data. This suggests that, when using a CH_4 homopause altitude of ~880 km, we must impose hydrodynamic methane escape rates in T-GITM to reproduce the INMS methane data. This is seen in Table 3 by comparing model B (HE), in which we impose a hydrodynamic-like escape rate of $\sim 2.60 \times 10^{13}$ CH_4 m^{-2} s^{-1}, with model B, where T-GITM simulates a methane escape rate of $\sim 3.15 \times 10^{11}$ CH_4 m^{-2} s^{-1}

Table 4. Arithmetic Percent Deviations Between the Average INMS Data and the T-GITM

	N_2 Density	CH_4 Density	H_2 Density	CH_4 Mixing	H_2 Mixing	^{40}Ar Mixing	$^{14}N/^{15}N$ Ratio
Section 4.1: Eddy diffusion tests with frozen temperatures							
Model A	5.8	6.6	4.5	4.1	5.6	12.7	0.8
Model B	5.3	100.5	5.5	84.0	6.0	36.6	8.2
Model B (HE)[a]	5.6	2.8	8.8	4.2	6.4	35.6	8.4
Section 4.2: Methane chemistry tests with frozen temperatures							
Model A	5.8	6.6	4.5	4.1	5.6	12.7	0.8
Model A (NC)[b]	5.9	40.1	4.9	30.9	5.8	12.1	0.9
Model A (NC HE)[ab]	6.0	9.2	4.5	6.4	5.5	12.6	0.8
Section 4.3: Energy balance calculations with $Q_{Plasma} = 3.04 \times 10^9$ (eV/cm^2/s)							
Model C	9.5	3.4	8.3	6.0	5.1	9.6	0.8
Model D	30.0	64.0	13.8	109.0	6.5	13.5	9.7
Model D (HE)[a]	53.0	30.9	24.1	40.9	99.0	48.0	11.6

[a](HE) means hydrodynamic escape rates are specified as a boundary condition.
[b](NC) means that simulation neglects methane chemical losses.

(referred to the surface of Titan). Meanwhile, model A (with a methane homopause of 990 km) can match INMS methane data while simulating methane escape rates of $\sim 1.41 \times 10^{11}$ CH_4 m^{-2} s^{-1}.

As seen in Figure 2c, the different T-GITM simulations match different ^{40}Ar data sets. Model A matches the mixing ratios derived by *Magee et al.* [2009], while models B and B (HE) both match those determined by *Yelle et al.* [2008]. Figure 2d contains a comparison between the isotopic ratios simulated by T-GITM and measured by INMS. As seen in this figure and as quantified in Table 4, model A represents a superior fit to these isotopic ratios. Moreover, as noted in *Mandt et al.* [2012], these isotope ratios possess lower counting statistical uncertainties and may function as a more reliable diagnostic for eddy diffusion than ^{40}Ar.

Figure 3 provides details about the dynamics and chemistry in models A, B, and B (HE). Figure 3a depicts the three species' velocities: N_2 is shown in black, CH_4 in red, and H_2 in blue. The different simulations are designated by the same line styles as they are in Figure 2. In Figure 3a, models A and B simulate consistent velocities for all of the species, suggesting that the main driver for the vertical dynamics (pressure-gravity balance) is largely the same. By contrast, the CH_4 velocities simulated by model B (HE) deviate significantly from the other two, due to the hydrodynamic escape rates specified at the upper boundary. This suggests that the CH_4 vertical dynamics in model B (HE) are driven by the hydrodynamic escape boundary condition rather than the physics within T-GITM.

Figure 3b depicts the vertical fluxes of H_2 (blue) and CH_4 (red) for each simulation as well as the limiting fluxes for both H_2 in light green and CH_4 in magenta. The H_2 fluxes (blue) in all three simulations are nearly identical and cannot be distinguished from one another. Due to the chemical production seen in Figure 3c (blue curves), the H_2 fluxes increase with altitude. The H_2 fluxes increase until they reach values very close to the H_2 limiting flux profile (green). After rising to meet the limiting flux curve between 900 and 1000 km altitude, the H_2 fluxes then become asymptotic, suggesting that the limiting flux is setting the eventual escape flux of H_2 out of the atmosphere—consistent with *Strobel* [2010, 2012] and *Cui et al.* [2008].

By contrast, the methane vertical fluxes show systematic differences between the three T-GITM simulations. First, we note that the CH_4 fluxes systematically decrease with altitude, due to the chemical destruction (red) shown in Figure 3c. For models A and B, the chemistry reduces the upward fluxes by over 2 orders of magnitude. By contrast, in the hydrodynamic escape case of model B (HE), T-GITM must adjust the lower boundary fluxes to accommodate both the chemistry and the imposed topside escape rates. As seen in Figure 3c, this combined effect causes the model B (HE) vertical methane fluxes (red dash-dotted line) to exceed the limiting fluxes (magenta dash-dotted line) between and 500 and 900 km, which then produces a decrease in the dash-dotted CH_4 volume mixing ratio seen in the prevoius Figure 2b.

Lastly, in Figure 3d we compare the eddy diffusion coefficients (gray) with both the methane (red) and molecular hydrogen (blue) molecular diffusion coefficients. The eddy diffusion coefficients for models B and B (HE) asymptote at a value of $K_{Max} = 1750.0$ m^2 s^{-1}, whereas model A does not reach its K_{Max} value listed in Table 3. The intersection altitude of K_E and D_{CH_4} defines the methane homopause altitudes listed in Table 3. Similarly, we note that the H_2 homopause occurs well below the region where the limiting fluxes are set, explaining why the simulated H_2 densities remain insensitive to the homopause altitude.

4.3. Impact of Methane Chemistry

Some studies suggest that methane chemistry does not significantly impact estimates for methane escape [cf. *Cui et al.*, 2012; *Strobel*, 2012; *Yelle et al.*, 2008]. However, *Bell et al.* [2011b] indicated that chemistry may play a pivotal role, and we now seek to isolate the impacts of including or excluding methane chemical destruction. For this purpose, we examine three more simulations: model A from Figures 2 and 3, a new model A (NC) that is identical to model A but ignores the chemical losses of methane (i.e., no chemistry, NC), and finally model A (NC HE) which is identical to model A (NC) but now includes specified hydrodynamic escape rates at the upper boundary (i.e., no chemistry, hydrodynamic escape, NC HE).

These three models use the same homopause altitude of 990 km, the same frozen thermal structure seen in Figure 1a, and the same composition constraints at 500 km used in section 4.2 and Table 2. Thus, only the column-integrated total methane chemistry and topside escape rates are being varied (listed in Table 3 and scaled relative to the surface). Note that, when we exclude the chemical losses of CH_4, we must still calculate the products of methane chemistry in order to capture H_2 production.

The results of this study are shown in Figure 4. In Figure 4a, we compare simulated CH_4 and H_2 mixing ratios (black) against the INMS data (red). While all of the models match the data to within the error bars shown,

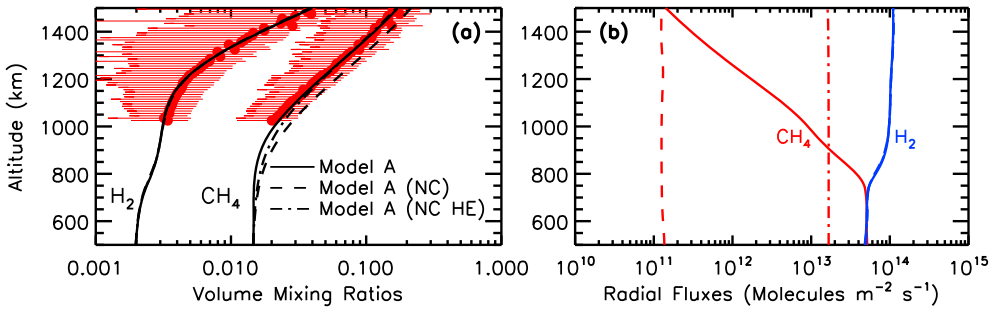

Figure 4. (a) Volume mixing ratios of methane and hydrogen, (b) their radial fluxes. Figure 4a shows methane chemistry study: model A, solid; model A (NC), dashed; and model A (NC HE), dash-dotted line. Red circles are data from *Magee et al.* [2009]. In Figure 4b, the red lines represent CH_4, and the blue lines represent H_2.

Table 4 shows that model A (NC) exhibits the highest deviation from the INMS measurements. By contrast, when hydrodynamic escape rates are imposed at the upper boundary in model A (NC HE), the simulated methane mixing ratios better reproduce the INMS data. Comparing models A (NC) and model A (NC HE) suggests that, when omitting methane chemical destruction, the only way to match INMS measurements is to impose hydrodynamic-like escape rates on the model. By contrast, model A is able to match the INMS methane mixing ratios with much lower methane escape rates, because it incorporates self-consistent chemical destruction of methane from direct photolytic, ion-neutral, and neutral-neutral chemistry [*Bell et al.*, 2010a, 2011b].

Figure 4b shows the vertical fluxes (scaled relative to the surface) for each species in the same format as Figure 3b. The vertical methane fluxes for model A (NC) and model A (NC HE) are constant with altitude (to within 1%), while model A shows the characteristic decrease with altitude due to the column-integrated chemical destruction of CH_4. Thus, these simulations also highlight that the methane chemistry has both compositional and dynamical impacts in the T-GITM simulations, emphasizing the highly coupled nature of Titan's upper atmosphere.

4.4. Coupled Energy Calculations

The T-GITM simulations in sections 4.1–4.3 were highly simplified by imposing a frozen temperature structure. However, this ignores the very important coupling between dynamics, composition, and energy balance. Thus, we next examine how estimates of CH_4 and H_2 atmospheric escape are altered by including the full Navier-Stokes equations in Appendix A by introducing three new T-GITM simulations: model C, a high-homopause simulation (990 km); model D, a low-homopause simulation (880 km); and model D (HE), a low-homopause simulation with hydrodynamic escape imposed. These new simulations are the analogues to models A, B, and B (HE) from section 4.1, as seen in Table 3.

For the self-consistent simulations, we include Solar EUV/UV heating, HCN rotational cooling, and finally a magnetospheric plasma heating term that was used in *Bell et al.* [2011a]. We use a fixed column-integrated magnetospheric plasma heating rate of 1.45×10^9 eV cm^{-2} s^{-1} (scaled relative to the surface) for all three simulations, which amounts to roughly 10% of the integrated solar EUV/UV heating (1.36×10^{10} eV cm^{-2} s^{-1}). Thus, models C, D, and D (HE) all share identical orbital, seasonal, and solar cycle parameters given in Table 1 and only the eddy diffusion coefficient and topside escape rates of methane are varying among these simulations (as seen in Table 3).

As seen in Figure 5, there is a systematic decrease in thermosphere temperatures going from model C to model D to model D (HE). Model C possesses the highest methane homopause of 990 km and the lowest escape rates of methane (see Table 3). The effects of this higher homopause altitude are evident in Figures 5b–5d. As was found in sections 4.2 and 4.3, the inclusion of the higher homopause altitude allows model C to match the CH_4 and ^{40}Ar mixing ratios without the need for hydrodynamic escape.

Model C also possesses the lowest simulated HCN mixing ratios in Figure 5d and most closely approximates the HCN mixing ratios measured by INMS as reported in *Magee et al.* [2009] (red vertical bar). This is because the higher turbulence transports HCN more efficiently downward through the model's lower boundary (i.e., into the lower atmosphere). HCN is considered to be the "thermostat" for Titan's upper atmosphere and efficiently cools the thermosphere through rotational line emission [*Yelle*, 1991]. Thus, less HCN abundances

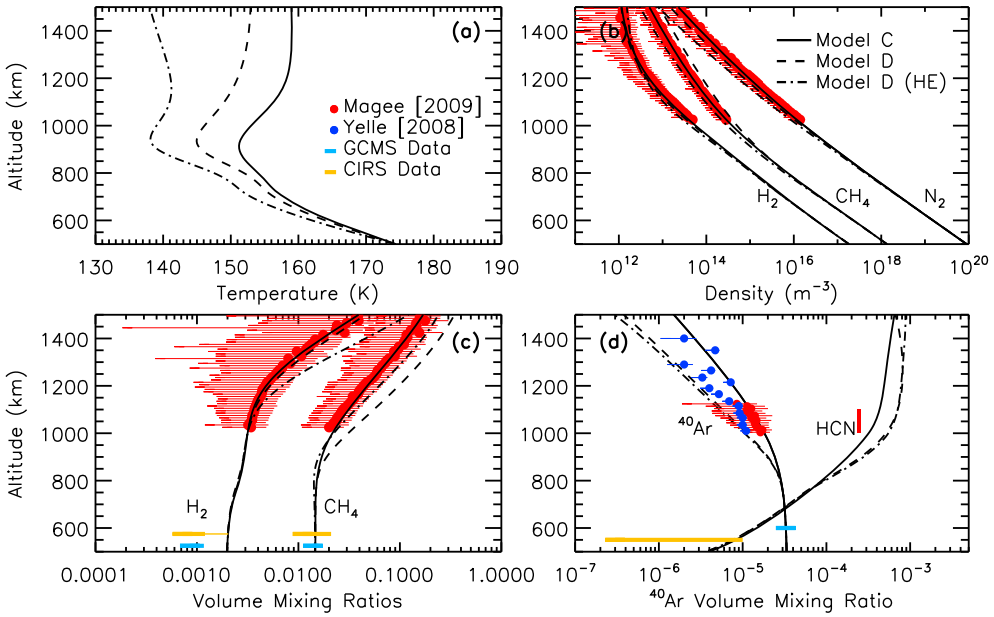

Figure 5. (a) Neutral temperatures, (b) neutral densities, (c) volume mixing ratios of methane and hydrogen, and (d) Argon mixing ratios. Shown are fully coupled Navier-Stokes simulations: model C, solid line; model D, dashed line, and model D (HE), dash-dotted line. Red data are from *Magee et al.* [2009], and blue data are from *Yelle et al.* [2008]. GCMS and CIRS constraints are cyan and yellow lines. The vertical red bar in Figure 5d is the INMS measurements of HCN reported in *Magee et al.* [2009].

in model C produce less radiative cooling and a warmer thermosphere. As indicated in *Magee et al.* [2009] the reported HCN mixing ratios are likely lower limits, due to antechamber sticking. Therefore, model C's overestimate of HCN values relative to those reported in *Magee et al.* [2009] is acceptable.

By contrast, the lower homopause altitudes in models D and D (HE) produce greater HCN mixing ratios above 1000 km, which increases the radiative cooling in the thermosphere and reduces the thermosphere temperatures in Figure 5a. These colder temperatures produce N_2, CH_4, and H_2 densities that do not match the INMS measurements as well as model C in Figures 5b and 5c. Even when including hydrodynamic escape in model D (HE), this model remains inferior to that of model C based upon its match to INMS data. Similarly, the H_2 mixing ratios in Figure 5c simulated by models D and D (HE) show increased deviations from INMS measurements due to the cold thermosphere temperatures that reduce thermal escape.

Finally, the major heating and cooling rates for the 1-D T-GITM are presented in Figure 6a in units of K s^{-1}, which capture the actual response of the simulated thermosphere to these different processes. As seen in Figure 6a and noted in *Bell et al.* [2010a], the dominant drivers for the thermosphere are the HCN cooling (blue) and the solar EUV/UV heating (red). Thermal conduction also plays a major role (black), as does a specified ion precipitation heating (magenta) that is adopted based upon the work by *Bell et al.* [2011a] and

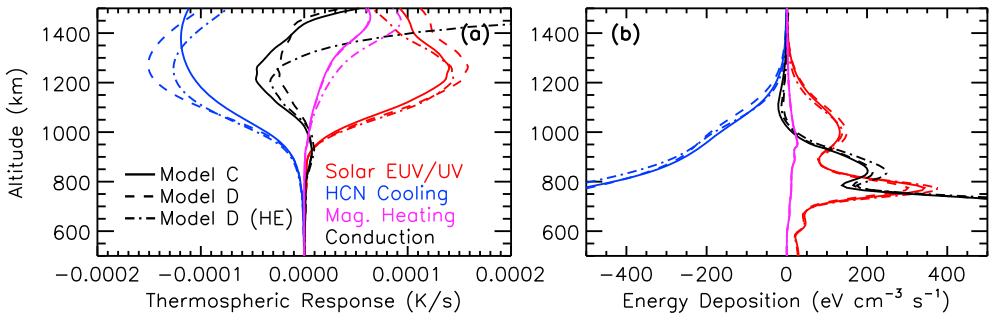

Figure 6. Energy balance terms. (a) The response of the thermosphere (in K s^{-1}) to the major heating and cooling processes. (b) Volume heating and cooling rates in eV cm^{-3} s^{-1}.

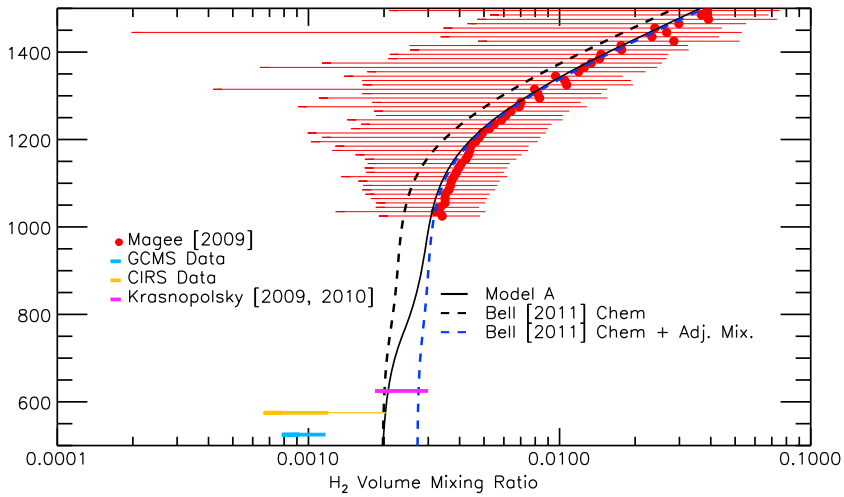

Figure 7. H_2 chemistry tests. Three T-GITM simulations are shown that use the Model C scaled chemistry (solid black), one that uses the *Bell et al.* [2010a] chemistry (dashed black), and one that uses the *Bell et al.* [2010a] chemistry with adjusted lower boundary mixing ratios. Red data points are from *Magee et al.* [2009], while the CIRS and GCMS H_2 constraints from the lower atmosphere are shown in yellow and cyan, respectively. The magenta horizontal lines bracket the range of H_2 mixing ratios simulated by both *Krasnopolsky* [2009] and *Krasnopolsky* [2010].

Westlake et al. [2011]. Figure 6b depicts the volume heating rates of the plasma heating (magenta) that have been adopted from the works of *Michael and Johnson* [2005], *Shah et al.* [2009], and *Smith et al.* [2009] along with the solar EUV/UV heating rates for comparison (red).

5. The Impacts of H_2 Chemistry

As with CH_4, quantifying H_2 escape by reproducing the observations of H_2 is central to understanding the evolutionary history of Titan's atmosphere. As noted in *Strobel* [2010, 2012], there is an apparent mismatch between the lower atmosphere and the upper atmosphere measurements of H_2. Essentially, 1-D models cannot reproduce the INMS H_2 measurements when using GCMS and/or CIRS constraints, and this difficulty can be seen in the H_2 mixing ratios of Figures 2 and 5. In these figures, we must use lower boundary H_2 mixing ratios in T-GITM that are higher than any measurements suggested by either CIRS (yellow horizontal lines) or GCMS (cyan lines). The horizontal CIRS range (yellow) also includes a factor of 2.0 enhancement in the near-surface H_2 mixing ratios in the midlatitudes to high latitudes reported by *Courtin et al.* [2008].

Next, we examine how variations in the H_2 chemical production can impact our ability to reconcile measurements of H_2 in the lower and upper atmosphere. As outlined in section 2, we have employed an empirical chemical production of H_2 given by $P_{H_2} = 1.15 \times L_{CH_4}$, which is loosely based upon the measurements of heavy hydrocarbon C:H ratios made by INMS [*Waite et al.*, 2007; *Westlake et al.*, 2012]. This scheme liberates significantly more H_2 than the original scheme of *Bell et al.* [2010a], and we now examine the implications of this added H_2 production on T-GITM simulated H_2 densities and mixing ratios.

In Figure 7, we compare three new T-GITM simulations that are identical to model A (high-methane homopause and fixed temperature), except that the H_2 chemistry and lower boundary conditions are altered in each case. The column-integrated H_2 production (scaled relative to the surface) is shown in Table 5. The baseline simulation is model A (shown in solid black). The second simulation is model A with the

Table 5. Integrated Hydrogen Chemistry (Scaled Relative to the Surface)

Simulation	Integrated Production
Model A	5.91×10^{13}
Model A with *Bell et al.* [2010a] chemistry	2.13×10^{13}
Model A with *Bell et al.* [2010a] + adjusted mixing ratio	2.08×10^{13}

semiempirical H_2 chemistry replaced with the scheme outlined in *Bell et al.* [2010a] (dashed black line), which liberates significantly less H_2 than the empirical method. The third simulation is model A with the *Bell et al.* [2010a] chemical scheme and an altered H_2 mixing ratio of 2.75×10^{-3} at 500 km, which is a mixing ratio consistent with previous work in *Bell et al.* [2010a] and *Strobel* [2010].

Figure 7 also shows the available constraints from the Huygens GCMS (light blue), the Cassini CIRS (yellow), and a range of mixing ratios from recent photochemical modeling studies in *Krasnopolsky* [2009] and *Krasnopolsky* [2010] (magenta). The data from GCMS and CIRS are obtained from much lower altitudes (near ~100–200 km), while the mixing ratio from the photochemical modeling are appropriate for 500 km. There are two primary observations to be made from this comparison. First, the semiempirical H_2 chemistry derived from the high-mass hydrocarbons allows T-GITM to match INMS using lower boundary mixing ratios that are closer to those measured by GCMS and CIRS deeper in the atmosphere. Second, when using the lower H_2 production of *Bell et al.* [2010a], we must adopt a higher lower boundary mixing ratio of H_2 that is consistent with recent photochemical models in the middle atmosphere but much higher than mixing ratios measured by either CIRS or GCMS.

6. Summary and Conclusions

Since the arrival of Cassini-Huygens to the Saturnian system, there has been an ongoing debate about the amount of CH_4 escape that is required by models to match the INMS data. These inferred CH_4 atmospheric escape rates have ranged from $\sim 1.0 \times 10^8$ CH_4 m^{-2} s^{-1} in *Bell et al.* [2010a, 2010b, 2011b] up to $\sim 2.0 \times 10^{13}$ CH_4 m^{-2} s^{-1} in *Yelle et al.* [2008], *Strobel* [2009, 2010, 2012], and *Cui et al.* [2012]. Moreover, *Strobel* [2012] and others maintain that the highest CH_4 escape rates are evidence of a hydrodynamic escape mechanism, although hydrodynamic escape is typically defined as the bulk outflow of the whole atmosphere in response to intense heating [cf. *Tian et al.*, 2008].

Our previous simulations in *Bell et al.* [2010a, 2010b, 2011b] demonstrated that hydrodynamic escape is only one possible model configuration consistent with INMS data. However, direct model-to-model comparisons between *Bell et al.* [2011b] and those such as *Strobel* [2010] were complicated by the fact that we included several factors including Sun-Saturn orbital distance variations over time as well as diurnal variations into our calculations which were ignored in the studies by *Yelle et al.* [2008], *Strobel* [2009, 2010, 2012], and *Cui et al.* [2012]. In the present work, we have reconfigured our T-GITM simulations to more closely approximate the approaches taken in other investigations into methane and molecular hydrogen escape.

When trying to reproduce the INMS data with models, It is well established that the amount of turbulence greatly impacts the amount of atmospheric methane escape required to match the INMS CH_4 data. Operationally, models parameterize turbulence using an adjustable eddy diffusion coefficient, and, thus, most studies use the inert gas ^{40}Ar to constrain it. When comparing different studies of atmospheric escape, one notices two major differences among them: (1) the method for including turbulence (i.e., how they parameterize it) and (2) the source for their ^{40}Ar data (either that of *Magee et al.* [2009] or *Cui et al.* [2008, 2012]). Fortunately, as seen in section 4.1 and Figure 1, the dynamical effects on ^{40}Ar are almost completely method invariant, whether you choose to use a hydrostatic diffusion approach (as in *Cui et al.* [2012] or *Yelle et al.* [2008]), include eddy diffusion in the continuity equation (as in *Strobel* [2009, 2010, 2012]), or include turbulence directly in the momentum equation (as in *Bell et al.* [2010a, 2010b, 2011b]). Thus, the primary differences among the various atmospheric escape studies must lie in the INMS ^{40}Ar mixing ratios used to constrain these eddy diffusion coefficients.

The large uncertainties in INMS retrieved ^{40}Ar mixing ratios are apparent in Figure 2c, which are so large that all of the simulated ^{40}Ar mixing ratios fall within this error range. These uncertainties in the ^{40}Ar data are due to (1) poor counting statistics, (2) the difficulty and nonuniqueness in subtracting other species, and (3) the relatively large geophysical variations from pass to pass. The end result is that a very minor species with very large uncertainties is being used almost exclusively to constrain turbulence effects in Titan's atmosphere. As an added complication, recent laboratory and Huygens probe data analysis has revealed that noble gases are efficiently "trapped" in Titan's atmospheric hazes [cf., *Bar-Nun et al.*, 2007, 2008, *Jacovi and Bar-Nun*, 2008]. Thus, in addition to very large observational uncertainties, ^{40}Ar is most likely not truly inert.

Mandt et al. [2012] suggested that the major stable isotopes of $^{14}N/^{15}N$ in N_2, when combined with ^{40}Ar, could provide improved constraints on turbulence. The authors point out that $^{14}N/^{15}N$ ratios possess

significantly improved counting statistics, which is evident in Figure 2d. As can be seen in Figure 2d and in Table 4, the models using a lower methane homopause, models B and B (HE), calculate isotope ratios outside the INMS uncertainties. Thus, when using the combination of ^{40}Ar and ^{14}N/^{15}N to constrain the eddy diffusion coefficient, we find that model A (high-methane homopause simulation) is superior to both models B and model B (HE).

Section 4.2 also reproduces and explains the results obtained by *Yelle et al.* [2008], *Cui et al.* [2009], and *Strobel* [2012]. These earlier studies maintain that the methane homopause is near 880 km, which is obtained by matching the blue data points in Figure 2c. As seen by comparing models B and B (HE), in order to match the INMS CH_4 data using this lower homopause altitude, we must then impose hydrodynamic escape rates of CH_4. This is what has been concluded by *Yelle et al.* [2008], *Cui et al.* [2009], and *Strobel* [2012].

In addition to turbulence, chemical destruction of methane also plays a major role in determining the amount of topside escape that is required by models to match INMS data. As seen in Figures 4a and 4b, when ignoring the methane chemistry T-GITM cannot match the INMS data without imposing hydrodynamic CH_4 escape rates on the model, since model A (NC HE) fits the data much better than model A (NC). This is essentially the same result obtained by *Yelle et al.* [2008] and *Cui et al.* [2012], who also ignore chemistry. Thus, when ignoring chemistry, one must compensate by imposing hydrodynamic outflow to match INMS data. By contrast, by including direct photolytic, neutral-neutral, and ion-neutral methane chemical losses, model A is able to match INMS data while simulating escape rates that are consistent with pre-Cassini estimates [see *Johnson et al.*, 2009].

Finally, including a self-consistent thermal balance calculation that responds to changing composition and dynamics further modifies estimates of atmospheric escape, as seen in section 4.4 and Figure 5. This section demonstrated that, as the homopause altitude decreases, the HCN mixing ratios increase, resulting in higher overall cooling of the thermosphere and highlighting the intimate connection between composition, dynamics, and energy balance. Because of this coupling, the lower methane homopause simulations—models D and D (HE)—did not match the available INMS measurements as well as the high-methane homopause simulation of model C (see Table 4). This thermal balance interplay has not been discussed before, since neither *Yelle et al.* [2008] nor *Cui et al.* [2012] include thermal balance calculations and *Strobel* [2012] does not include the self-consistent HCN chemistry.

In contrast to CH_4, H_2 escape is comparatively simple. When freezing the thermal structure, the H_2 escape rates required to match INMS data are given by classical Jeans escape, which is consistent with recent kinetic modeling by *Tucker et al.* [2012]. Moreover, when freezing the thermal structure, H_2 is invariant to our choice of methane homopause, which conflicts with the findings of *Strobel* [2012] who suggested that a high-methane homopause impacted simulated hydrogen densities. In fact, when examining the fully self-consistent T-GITM simulations of section 4.4, we find that model C, which has the highest methane homopause, best reproduces the measured H_2 densities and mixing ratios. Finally, the results in section 5 reveal that, for a given thermal structure, simulated H_2 densities are most sensitive to the chemical scheme used. If we liberate more H_2 from chemistry, then we are better able to reconcile lower and upper atmosphere H_2 measurements, suggesting that the key to reconciling the GCMS and CIRS H_2 measurements with INMS data lies in the chemical scheme used.

Ultimately, we have demonstrated that it is possible to reconcile simultaneously both the lower and upper atmosphere measurements of CH_4 and H_2 and that there is no need for hydrodynamic escape of methane. Our best fit configurations of T-GITM (models A and C) have methane homopauses near 990 km, and they match both lower and upper atmospheric measurements of CH_4, ^{40}Ar, HCN, and the ^{14}N/^{15}N isotopic ratio in N_2. Our estimates of upwelling methane fluxes are at most $\sim 1.5 \times 10^{11}$ CH_4 m^{-2} s^{-1} (or $\sim 10^{25}$ CH_4 s^{-1} globally), which is consistent with recent nonthermal escape rates estimated by *De La Haye et al.* [2008] and *Johnson et al.* [2009]. Moreover, these are global mean upper limits on neutral methane escape, since (1) T-GITM likely underestimates methane chemical losses and (2) kinetic treatments are needed to estimate actual escape fluxes (such as *Tucker and Johnson* [2009] or *Tucker et al.* [2012]). Finally, our studies suggest that the key to reconciling the apparent mismatch between lower and upper atmospheric measurements of H_2 lies in the complex chemistry of Titan's atmosphere between 200 km and 1000 km.

Appendix A: Methods for Including Eddy Diffusion

The Titan-Global Ionosphere-Thermosphere Model (T-GITM) solves the time-dependent, coupled Navier-Stokes continuity, momentum, and energy equations outlined in *Bell et al.* [2010a]. We assume that each neutral species possesses its own continuity equation and its own vertical velocity (radial velocity). However, T-GITM assumes that all neutral species share the same background temperature [*Ridley et al.*, 2006]. The continuity equation is given by

$$\frac{\partial \rho_s}{\partial t} + \nabla \cdot \left(\rho_s \mathbf{u}_s\right) = P_s - L_s, \tag{A1}$$

where ρ_s represents the mass density (kg m^{-3}), $\mathbf{u}_s$ the velocity (m s^{-1}), P_s the chemical sources (kg m^{-3} s^{-1}), and finally L_s the chemical losses (kg m^{-3} s^{-1}) for a species, "*s*." Next, the species-specific momentum equation is given by

$$\rho_s \frac{\partial \mathbf{u}_s}{\partial t} + \rho_s \mathbf{u}_s \cdot \nabla \mathbf{u}_s + \nabla p_s + \nabla \cdot \tau_s - \rho_s \mathbf{g} + \rho_s \left[2\boldsymbol{\Omega}_r \times \mathbf{u}_s + \boldsymbol{\Omega}_r \times \left(\boldsymbol{\Omega}_r \times r\right)\right] = \sum_{t \neq s} \rho_s \nu_{st} \left(\mathbf{u}_t - \mathbf{u}_s\right) + \sum_{t \neq s} \rho_s \nu_{st} \left(\boldsymbol{\omega}_s - \boldsymbol{\omega}_t\right). \tag{A2}$$

In equation (A2), τ_s is the velocity stress tensor (in Pa), $\mathbf{g}$ the gravitational acceleration (in m s^{-2}), $\boldsymbol{\Omega}_r$ Titan's rotational angular velocity (rads s^{-1}), ν_{st} the momentum collision frequency (s^{-1}), and $\boldsymbol{\omega}_s$ the eddy diffusion velocity (in m s^{-1}). The eddy diffusion velocity is given by *Colegrove et al.* [1966] as

$$\omega_s = -K_E(r) \frac{1}{\chi_s} \frac{\partial \chi_s}{\partial r}, \tag{A3}$$

where $K_E(r)$ is the eddy diffusion coefficient and χ_s is the species' volume mixing ratio. Finally, the energy equation solved by T-GITM is given by

$$\frac{\partial T}{\partial t} + \mathbf{u} \cdot \nabla T + (\gamma - 1)\, T\, (\nabla \cdot \mathbf{u}) + \frac{\tau : \nabla \mathbf{u}}{\rho\, c_v} = \frac{1}{\rho c_v} \left(Q_{\text{Total}} - \nabla \cdot \mathbf{q}\right). \tag{A4}$$

Here T represents the bulk background temperature (K), $\mathbf{u}$ the mass-weighted mean velocity, τ the mean velocity stress tensor, ρ the mean mass density, c_v the specific heat at a constant volume (J kg^{-1} K^{-1}), Q_{Total} is the total energy sources in units of (W m^{-3}), and $\mathbf{q}$ thermal conduction. Q_{Total} has several contributions, including solar EUV/UV heating, HCN rotational cooling, and magnetospheric ion precipitation heating, such that $Q_{\text{Total}} = Q_{\text{EUV}} + Q_{\text{Plasma}} - Q_{\text{HCN}}$. We close the Navier-Stokes equations with the collision-dominated versions of the viscosity stress tensor and heat flux vector as follows:

$$\tau_s = \eta_s \left[\nabla \mathbf{u}_s + \left(\nabla \mathbf{u}_s\right)^T - \frac{2}{3} \left(\nabla \cdot \mathbf{u}_s\right) I\right], \tag{A5}$$

$$\mathbf{q} = -\lambda \nabla T, \tag{A6}$$

where λ is the thermal conduction coefficient (W m^{-1} K^{-1}), η_s is the viscosity coefficient (kg m^{-1} s^{-1}), and I is the second-order unit tensor.

Next, we outline three methods for including turbulence in 1-D simulations of Titan's upper atmosphere. The first method is shown above in equations (A1)–(A3), where we include the effects of turbulence directly in the momentum equation, as done by both *Bell et al.* [2010a] and *Boqueho and Blelly* [2005]. This is our preferred method and is denoted "GITM Momentum Eqn" in Figure 1. A second method for dealing with turbulence is to use a purely hydrostatic diffusion approach consistent with *Cui et al.* [2012], *Yelle et al.* [2006], and *Yelle et al.* [2008]:

1. Continuity

$$\nabla \cdot \left(\Phi_s\right) = 0. \tag{A7}$$

2. Momentum

$$\frac{1}{\chi_s} \frac{\partial \chi_s}{\partial r} = \frac{D_s}{D_s + K_E} \left[\frac{1}{H_{\text{atm}}} - \frac{1}{H_s}\right] \left(1 - \frac{\Phi_s}{\Phi_{I,s}}\right). \tag{A8}$$

3. Diffusion limited flux

$$\Phi_{l,s} = D_s N \left(\frac{1}{H_{\text{atm}}} - \frac{1}{H_s} \right) \chi_s. \tag{A9}$$

4. Hydrostatic equilibrium of the atmosphere

$$\frac{1}{N}\frac{\partial N}{\partial r} + \frac{1}{T}\frac{\partial T}{\partial r} = -\left(\frac{1}{H_{\text{atm}}} \right). \tag{A10}$$

In these expressions, Φ_s is the species-specific flux (in molecules m^{-2} s^{-1}), where $\Phi_s = n_s v_s$ and $\Phi_{l,s}$ represents the diffusion limited flux of *Hunten* [1973]. H_{atm} is the atmospheric scale height (in m), and H_s is the species-specific scale height. D_s represents the total diffusion coefficient for species "*s*" (in m^2 s^{-1}). All other variables are the same as in equations (A1)–(A4). This approach is denoted "Diffusion Eqn" in Figure 1.

The third and final method approximates that of *Strobel* [2009, 2010, 2012], who includes turbulence effects in the continuity equation:

1. Continuity

$$\frac{\partial \rho_s}{\partial t} + \nabla \cdot \left(\rho_s \mathbf{u}_s + \rho_s \omega_s \right) = 0.0. \tag{A11}$$

2. Momentum

$$\rho_s \frac{\partial \mathbf{u}_s}{\partial t} + \rho_s \mathbf{u}_s \cdot \nabla \mathbf{u}_s + \nabla p_s + \nabla \cdot \tau_s - \rho_s \mathbf{g} + = \sum_{t \neq s} \rho_s \nu_{st} \left(\mathbf{u}_t - \mathbf{u}_s \right). \tag{A12}$$

where all of the variables are the same as in the standard T-GITM formulation in equations (A1)–(A4). This method is denoted as "GITM Continuity Eqn" in Figure 1.

Acknowledgments

J. Bell would like to thank A. Nagy and all of the INMS team members for their input and guidance. Also, the authors would like to thank the Center for Space Environment Modeling (CSEM) at the University of Michigan for continued use of their computational facilities and expertise. This work was supported by the NASA grant NAS703001NM0710023, subcontracted through JPL. The NASA High End Computing (HEC) and the University of Texas Advanced Computing Center (TACC) supported the simulations presented here.

Michael Balikhin thanks Thomas Cravens and Philippe Garnier for their assistance in evaluating this paper.

References

Achterberg, R. K., B. J. Conrath, P. J. Gierasch, F. M. Flasar, and C. A. Nixon (2008), Titan's middle-atmospheric temperatures and dynamics observed by the Cassini Composite Infrared Spectrometer, *Icarus*, *194*, 263–277, doi:10.1016/j.icarus.2007.09.029.

Atreya, S. K. (1986), *Atmospheres and Ionospheres of the Outer Planets and Their Satellites*, 15, Springer Series on Physics Chemistry Space, Springer Verlag, Berlin, Germany.

Bar-Nun, A., G. Notesco, and T. Owen (2007), Trapping of N_2, CO and Ar in amorphous ice application to comets, *Icarus*, *190*, 655–659, doi:10.1016/j.icarus.2007.03.021.

Bar-Nun, A., V. Dimitrov, and M. Tomasko (2008), Titan's aerosols: Comparison between our model and DISR findings, *Planet. Space Sci.*, *56*, 708–714, doi:10.1016/j.pss.2007.11.014.

Bell, J. M., J. Westlake, and J. H. Waite (2011a), Simulating the time-dependent response of Titan's upper atmosphere to magnetospheric forcing, *Geophys. Res. Lett.*, *38*, L06202, doi:10.1016/2010GL046420.

Bell, J. M., et al. (2010a), Simulating the one-dimensional structure of Titan's upper atmosphere: 1. Formulation of the Titan Global Ionosphere-Thermosphere Model and benchmark simulations, *J. Geophys. Res.*, *115*, E12002, doi:10.1029/2010JE003636.

Bell, J. M., et al. (2010b), Simulating the one-dimensional structure of Titan's upper atmosphere: 2. Alternative scenarios for methane escape, *J. Geophys. Res.*, *115*, E12018, doi:10.1029/2010JE003638.

Bell, J. M., et al. (2011b), Simulating the one-dimensional structure of Titan's upper atmosphere: 3. Mechanisms determining methane escape, *J. Geophys. Res.*, *116*, E11002, doi:10.1029/2010JE003639.

Boqueho, V., and P.-L. Blelly (2005), Contributions of a multimoment multispecies approach in modeling planetary atmospheres: Example of Mars, *J. Geophys. Res.*, *110*, A01313, doi:10.1029/2004JA010414.

Clarke, D. W., and J. P. Ferris (1997), Chemical evolution on Titan: Comparisons to the prebiotic Earth, *Origins Life Evol. Biosphere*, *27*, 225–248.

Colegrove, F. D., F. S. Johnson, and W. B. Hanson (1966), *Atmospheric Composition in the Lower Thermosphere*, 2227–2236, vol. 71.

Courtin, R. D., C. Sim, S. Kim, D. Gautier, and D. E. Jennings (2008), Latitudinal variations of tropospheric H_2 on Titan from the Cassini CIRS investigation, *AAS/Division for Planetary Sciences Meeting Abstracts #40, Bulletin of the American Astronomical Society*, vol. 40, p. 446.

Cui, J., R. V. Yelle, and K. Volk (2008), Distribution and escape of molecular hydrogen in Titan's thermosphere and exosphere, *J. Geophys. Res.*, *113*, E10004, doi:10.1029/2007JE003032.

Cui, J., R. V. Yelle, D. F. Strobel, I. C. F. Muller-Wodarg, D. S. Snowden, T. T. Koskinen, and M. Galand (2012), The CH_4 structure in Titan's upper atmosphere revisited, *J. Geophys. Res.*, *117*, E11006, doi:10.1029/2012JE004222.

Cui, J., et al. (2009), Analysis of Titan's neutral upper atmosphere from Cassini Ion Neutral Mass Spectrometer measurements, *Icarus*, *200*, 581–615, doi:10.1016/j.icarus.2008.12.005.

De La Haye, V., J. H. Waite, T. E. Cravens, I. P. Robertson, and S. Lebonnois (2008), Coupled ion and neutral rotating model of Titan's upper atmosphere, *Icarus*, *197*, 110–136, doi:10.1016/j.icarus.2008.03.022.

Flasar, F. M., et al. (2005), Titan's atmospheric temperatures, winds, and composition, *Science*, *308*, 975–978, doi:10.1126/science.1111150.

Fulchignoni, M., et al. (2005), In situ measurements of the physical characteristics of Titan's environment, *Nature*, *438*, 785–791, doi:10.1038/nature04314.

Hunten, D. M (1973), The escape of H_2 from Titan, *J. Atmos. Sci.*, *30*, 726–732.
Hunten, D. M (1974), The escape of light gases from planetary atmospheres, *J. Atmos. Sci.*, *30*, 1481–1494.
Jacovi, R., and A. Bar-Nun (2008), Removal of Titan's noble gases by their trapping in its haze, *Icarus*, *196*, 302–304, doi:10.1016/j.icarus.2008.02.014.
Jennings, D. E., et al. (2009), Titan's surface brightness temperatures, *Astrophys. J.*, *691*, L103–L105, doi:10.1088/0004-637X/691/2/L103.
Johnson, R. E., O. J. Tucker, M. Michael, E. C. Sittler, D. T. Young, and J. H. Waite (2009), Mass loss processes in Titan's upper atmosphere, in *Titan After Cassini-Huygens*, edited by R. Brown, pp. 373–391, Chapter 15, Springer, Netherlands.
Krasnopolsky, V. A. (2009), A photochemical model of Titan's atmosphere and ionosphere, *Icarus*, *201*, 226–256, doi:10.1016/j.icarus.2008.12.038.
Krasnopolsky, V. A. (2010), The photochemical model of Titan's atmosphere and ionosphere: A version without hydrodynamic escape, *Planet. Space Sci.*, *58*, 1507–1515, doi:10.1016/j.pss.2010.07.010.
Liou, M.-S. (2006), A sequel to AUSM, Part II: AUSM $^+$-up for all speeds, *J. Comput. Phys.*, *214*, 137–170, doi:10.1016/j.jcp.2005.09.020.
Lorenz, R. D., C. P. McKay, and J. I. Lunine (1999), Analytic investigation of climate stability on Titan: Sensitivity to volatile inventory, *Planet. Space Sci.*, *47*, 1503–1515, doi:10.1016/S0032-0633(99)00038-0.
Magee, B. A., J. H. Waite, K. E. Mandt, J. Westlake, J. Bell, and D. A. Gell (2009), INMS-derived composition of Titan's upper atmosphere: Analysis methods and model comparison, *Planet. Space Sci.*, *57*, 1895–1916, doi:10.1016/j.pss.2009.06.016.
Mandt, K. E., J. H. Waite, W. Lewis, B. Magee, J. Bell, J. Lunine, O. Mousis, and D. Cordier (2009), Isotopic evolution of the major constituents of Titan's atmosphere based on Cassini data, *Planet. Space Sci.*, *57*, 1917–1930, doi:10.1016/j.pss.2009.06.005.
Mandt, K. E., et al. (2012), Ion densities and composition of Titan's upper atmosphere derived from the Cassini Ion Neutral Mass Spectrometer: Analysis methods and comparison of measured ion densities to photochemical model simulations, *J. Geophys. Res.*, *117*, E10006, doi:10.1029/2012JE004139.
Michael, M., and R. E. Johnson (2005), Energy deposition of pickup ions and heating of Titan's atmosphere, *Planet. Space Sci.*, *53*, 1510–1514, doi:10.1016/j.pss.2005.08.001.
Niemann, H. B., et al. (2010), Composition of Titan's lower atmosphere and simple surface volatiles as measured by the Cassini-Huygens probe gas chromatograph mass spectrometer experiment, *J. Geophys. Res.*, *115*, 1E12006, doi:10.1029/2010JE003659.
Ridley, A. J., Y. Deng, and G. Tóth (2006), The global ionosphere thermosphere model, *J. Atmos. Terr. Phys.*, *68*, 839–864, doi:10.1016/j.jastp.2006.01.008.
Sagan, C., and W. R. Thompson (1984), Production and condensation of organic gases in the atmosphere of Titan, *Icarus*, *59*, 133–161, doi:10.1016/0019-1035(84)90018-6.
Shah, M. B., C. J. Latimer, E. C. Montenegro, O. J. Tucker, R. E. Johnson, and H. T. Smith (2009), The implantation and interactions of O^+ in Titan's atmosphere: Laboratory measurements of collision-induced dissociation of N_2 and modeling of positive ion formation, *Astrophys. J.*, *703*, 1947, doi:10.1088/0004-637X/703/2/1947.
Smith, H. T., R. E. Johnson, M. E. Perry, A. M. Rymer, and T. A. Cassidy (2009), The influence of neutrals on Saturn's magnetosphere. *Magnetospheres of the Outer Planets (MOP) abstracts*.
Strobel, D. F. (2008), Titan's hydrodynamically escaping atmosphere, *Icarus*, *193*, 588–594, doi:10.1016/j.icarus.2007.08.014.
Strobel, D. F. (2009), Titan's hydrodynamically escaping atmosphere: Escape rates and the structure of the exobase region, *Icarus*, *202*, 632–641, doi:10.1016/j.icarus.2009.03.007.
Strobel, D. F. (2010), Molecular hydrogen in Titan's atmosphere: Implications of the measured tropospheric and thermospheric mole fractions, *Icarus*, *208*, 878–886, doi:10.1016/j.icarus.2010.03.003.
Strobel, D. F. (2012), Hydrogen and methane in Titan's atmosphere: Chemistry, diffusion, escape, and the Hunten limiting flux principle. 11 This article is part of a Special Issue that honours the work of Dr. Donald M. Hunten FRSC who passed away in December 2010 after a very illustrious career, *Can. J. Phys.*, *90*, 795–805, doi:10.1139/p11-131.
Teanby, N. A., et al. (2007), Vertical profiles of HCN, HC_3N, and C_2H_2 in Titan's atmosphere derived from Cassini/CIRS data, *Icarus*, *186*, 364–384, doi:10.1016/j.icarus.2006.09.024.
Tian, F., J. F. Kasting, H. Liu, and R. G. Roble (2008), Hydrodynamic planetary thermosphere model: 1. Response of the Earth's thermosphere to extreme solar EUV conditions and the significance of adiabatic cooling, *J. Geophys. Res.*, *113*, E05008, doi:10.1029/2007JE002946.
Tucker, O. J., and R. E. Johnson (2009), Thermally driven atmospheric escape: Monte Carlo simulations for Titan's atmosphere, *Planet. Space Sci.*, *57*, 1889–1894, doi:10.1016/j.pss.2009.06.003.
Tucker, O. J., J. T. Erwin, J. I. Deighan, A. N. Volkov, and R. E. Johnson (2012), Thermally driven escape from Pluto's atmosphere: A combined fluid/kinetic model, *Icarus*, *217*, 408–415, doi:10.1016/j.icarus.2011.11.017.
Tucker, O. J., R. E. Johnson, J. I. Deighan, and A. N. Volkov (2013), Diffusion and thermal escape of H_2 from Titan's atmosphere: Monte Carlo simulations, *Icarus*, *222*, 149–158, doi:10.1016/j.icarus.2012.10.016.
Ullrich, P. A., and C. Jablonowski (2012), MCore: A non-hydrostatic atmospheric dynamical core utilizing high-order finite-volume methods, *J. Comput. Phys.*, *231*, 5078–5108, doi:10.1016/j.jcp.2012.04.024.
Waite, J. H., D. T. Young, T. E. Cravens, A. J. Coates, F. J. Crary, B. Magee, and J. Westlake (2007), The process of tholin formation in Titan's upper atmosphere, *Science*, *316*, 870–875, doi:10.1126/science.1139727.
Westlake, J. H., J. M. Bell, J. H. Waite, R. E. Johnson, J. G. Luhmann, B. A. Magee, K. E. Mandt, and A.-M. Rymer (2011), Titan's thermospheric response to various plasma environments, *J. Geophys. Res.*, *116*, A03318, doi:10.1029/2010JA016251.
Westlake, J. H., J. H. Waite Jr., K. E. Mandt, N. Carrasco, J. M. Bell, B. A. Magee, and J.-E. Wahlund (2012), Titan's ionospheric composition and structure: Photochemical modeling of Cassini INMS data, *J. Geophys. Res.*, *117*(E1), E01003, doi:10.1029/2011JE003883.
Yelle, R. V. (1991), Non-LTE models of Titan's upper atmosphere, *Astrophys. J.*, *383*, 380–400, doi:10.1086/170796.
Yelle, R. V., N. Borggren, V. de La Haye, W. T. Kasprzak, H. B. Niemann, I. Müller-Wodarg, and J. H. Waite (2006), The vertical structure of Titan's upper atmosphere from Cassini Ion Neutral Mass Spectrometer measurements, *Icarus*, *182*, 567–576, doi:10.1016/j.icarus.2005.10.029.
Yelle, R. V., J. Cui, and I. C. F. Müller-Wodarg (2008), Methane escape from Titan's atmosphere, *J. Geophys. Res.*, *113*, E10003, doi:10.1029/2007JE003031.
Yung, Y. L., and W. B. Demore (Ed.) (1999), *Photochemistry of Planetary Atmospheres*, Oxford Univ. Press, Oxford, U. K.
Yung, Y. L., M. Allen, and J. P. Pinto (1984), Photochemistry of the atmosphere of Titan: Comparison between model and observations, *Astrophys. J. Supp.*, *55*, 465–506, doi:10.1086/190963.